Journal of Aerosol Science 90 (2015) 169–181

Contents lists available at ScienceDirect

Journal of Aerosol Science

journal homepage: www.elsevier.com/locate/jaerosci

Measurement of transport properties of aerosolized nanomaterials

Bon Ki Ku*, Pramod Kulkarni

Centers for Disease Control and Prevention (CDC), National Institute for Occupational Safety and Health (NIOSH), Division of Applied Research and Technology (DART), 1090 Tusculum Ave, MS-R3, Cincinnati, OH 45226, USA

ARTICLE INFO

Article history:
Received 24 April 2015
Received in revised form
26 August 2015
Accepted 1 September 2015
Available online 10 September 2015

Keywords:
Transport properties
Aerosolized nanomaterials
Morphological descriptors
Principal component analysis

ABSTRACT

Airborne engineered nanomaterials such as single-walled carbon nanotubes (SWCNTs), multi-walled carbon nanotubes (MWCNTs), functionalized MWCNT, graphene, fullerene, silver and gold nanorods were characterized using a tandem system of a differential mobility analyzer and an aerosol particle mass analyzer to obtain their airborne transport properties and understand their relationship to morphological characteristics. These nanomaterials were aerosolized using different generation methods such as electrospray, pneumatic atomization, and dry aerosolization techniques, and their airborne transport properties such as mobility and aerodynamic diameters, mass scaling exponent, dynamic shape factor, and effective density were obtained. Laboratory experiments were conducted to directly measure mobility diameter and mass of the airborne nanomaterials using tandem mobility-mass measurements. Mass scaling exponents, aerodynamic diameters, dynamic shape factors and effective densities of mobility-classified particles were obtained from particle mass and the mobility diameter. Microscopy analysis using Transmission Electron Microscopy (TEM) was performed to obtain morphological descriptors such as envelop diameter, open area, aspect ratio, and projected area diameter. The morphological information from the TEM was compared with measured aerodynamic and mobility diameters of the particles. The results showed that aerodynamic diameter is smaller than mobility diameter below 500 nm by a factor of 2–4 for all nanomaterials except silver and gold nanorods. Morphologies of MWCNTs generated by liquid-based method, such as pneumatic atomization, are more compact than those of dry dispersed MWCNTs, indicating that the morphology depends on particle generation method. TEM analysis showed that projected area diameter of MWCNTs appears to be in reasonable agreement with mobility diameter in the size range from 100 to 400 nm. Principal component analysis of the obtained airborne particle properties also showed that the mobility diameter-based effective density and aerodynamic diameter are eigenvectors and can be used to represent key transport properties of interest.

Published by Elsevier Ltd.

1. Introduction

There is a growing concern over the potential health risks from exposure to airborne nanomaterials in industrial environments. Respiratory deposition of airborne nanomaterials following exposure to them during manufacturing and handling in

* Corresponding author. Tel.: +1 513 841 4147; fax: +1 513 841 4545.
E-mail address: BKu@cdc.gov (B.K. Ku).

http://dx.doi.org/10.1016/j.jaerosci.2015.09.001
0021-8502/Published by Elsevier Ltd.

the workplace is also of high concern (NIOSH, 2009, 2013). Although nanomaterials with unique physical/chemical properties and structures such as carbon nanotubes, graphene, and silver nanoparticles are gaining more attention for application to medical sensors, nanocomposite materials, and electronic devices (Baughman, Zakhidov, & de Heer, 2002; Hajipour, Fromm, Ashkarran, de Aberasturi, & de Larramendi, 2012; Novoselov et al., 2012), recent toxicological studies of fibrous nanostructured materials such as carbon nanotube and nanofibers have shown that these materials are associated with fibrotic lung responses, and result in inflammation and an increased risk of carcinogenesis (Kisin et al., 2011; Mercer et al., 2013; Sargent et al., 2014; Shvedova et al., 2005). Recent studies have shown that airborne particles emitted from manufacturing process of carbon nanofibers (CNF) in a workplace have either fibrous or agglomerated morphology structures with a dominant modal diameter of 200–250 nm in both mobility and aerodynamic diameters, and that chemical components of the aerosols consist of elemental carbon, iron-rich soot, and a mixture of these (Birch, Ku, Evans, & Ruda-Eberenz, 2011; Evans, Ku, Birch, & Dunn, 2010). In addition, studies have shown that airborne single-walled carbon nanotubes (SWCNTs) released during simulated work practices involving handling of large quantities of their dry powders are mainly agglomerates, not single fibers (Maynard et al., 2004). These agglomerates have nanoscale as well as macroscale features; they typically possess low overall aspect ratios, often less than 3–5, and have porous structures with extremely high surface area-to-mass ratio. According to the inertial impactor measurements, it was shown that the overall enveloping physical size of airborne SWCNT agglomerates is much larger than their aerodynamic size, by a factor of up to 10 (Baron et al., 2008). This implies that their diffusion-equivalent size could be much larger than their aerodynamic size. Therefore, lung dosimetry calculations of these materials based on aerodynamic size using particle dosimetry models, such as the ICRP Model (1994) and the Multiple Path Particle Dosimetry (MPPD) model (Anjilvel & Asgharian, 1995), would overestimate total particulate dose below 500 nm. Therefore, relevant equivalent diameters must be used to obtain reliable estimation of lung deposition fraction.

The objective of this study was to measure transport properties of various airborne engineered nanomaterials such as SWCNTs, multi-walled carbon nanotubes (MWCNTs), functionalized MWCNTs, graphene, fullerene, and silver or gold nanorods, and also, to characterize their morphological descriptors to find a relationship among their transport properties and morphology-based descriptors. Laboratory experiments were designed and conducted to measure diffusion diameter and mass of airborne nanomaterial aerosols generated using different techniques by tandem mobility-mass approach.

2. Transport properties and morphological descriptors

Fundamental transport properties such as mobility and mass of aerosolized nanomaterials were directly measured using tandem mobility-mass approach (Ku, Emery, Maynard, Stolzenburg, & McMurry, 2006; McMurry, Wang, Park, & Ehara, 2002). The other properties and equivalent diameters were obtained using relationships among the measured mobility diameter, mass, and the property of interest. The deduced properties include effective density, aerodynamic diameter, mass scaling exponent, and dynamic shape factor. Descriptors of morphological characteristics were obtained by image analysis of Transmission Electron Microscopy (TEM) micrographs. The morphological descriptors consist of envelop diameter, open area, aspect ratio, and projected area equivalent diameter. Explanation and definition of these properties are made in the following.

2.1. Transport properties

1. Effective density – the effective density of a particle used in our study is defined as the particle mass divided by the particle volume based on mobility diameter (McMurry et al., 2002).

$$\rho_{eff} = \frac{6m_p}{\pi d_{mob}^3} \tag{1}$$

where ρ_{eff} is the effective density, m_p is the particle mass, and d_{mob} is electrical mobility diameter.

2. Aerodynamic diameter – this diameter is obtained from the relationship among mobility diameter, mass, and effective density (Park, Cao, Kittelson, & McMurry, 2003):

$$d_{ae}^2 C(d_{ae}) = \frac{\rho_{eff} d_{mob}^2 C(d_{mob})}{\rho_0}. \tag{2}$$

where d_{ae} is the aerodynamic diameter, ρ_0 is the standard reference density of a particle (1.0 g cm^{-3}), and $C(d_{ae})$ and $C(d_{mob})$ are slip correction factors using d_{ae} and d_{mob}, respectively. The aerodynamic diameter was obtained by an iterative solution.

3. Mass scaling exponent – we use a term "mass scaling exponent" instead of a fractal dimension, because it is not known if the particles used in this study are pure fractals. However, the mass scaling exponent of a particle is analogous to the fractal dimension of pure fractals (Schmidt-ott, Baltensperger, Gaggeler, & Jost, 1990):

$$m_p \sim d_{mob}^{D_f} \tag{3}$$

where D_f is the mass scaling exponent.

4. Dynamic shape factor (DSF) – The dynamic shape factor is defined as the ratio of the actual resistance force of the nonspherical particle to the resistance force of a sphere having the same volume and velocity as the nonspherical particle (Hinds, 1999). The dynamic shape factor with slip correction in the transition regime is given by (Kasper, 1982; Kulkarni et al., 2011)

$$X = \frac{d_{mob} C(d_{ve})}{d_{ve} C(d_{mob})} \tag{4}$$

where d_{ve}, volume equivalent diameter, is the diameter of a sphere having the same volume as that of the irregular particle. $C(d_{ve})$ is the slip correction factor for d_{ve}. The volume equivalent diameter d_{ve} is obtained from mass and particle material density (ρ_p), which is known to be ~ 2.0 g cm^{-3} for MWCNTs used in this study (Nanoamor Inc., 2015).

$$d_{ve} = \left(\frac{6m_p}{\pi \rho_p}\right)^{1/3} \tag{5}$$

2.2. Morphological descriptors from TEM analysis

Envelop diameter was defined as a diameter of a sphere with the same projected area as that of a smallest ellipse which inscribes the particle of interest. Fig. S1 shows how to obtain the envelop diameter from TEM image of a particle. A Digital Micrograph (DM) software (ver 3.11.2, Gatan Inc., Pleasanton, CA) was used for image analysis (e.g., see Fig. S1). Once the ellipse is found, the area and major and minor axes of the ellipse were obtained for further analysis.

Aspect ratio was defined as a ratio of major axis to minor axis of the smallest ellipse which inscribes the particle of interest. It is worth noting that the aspect ratio defined in this way is different from the definition for aspect ratio of a single fiber which is defined as the ratio of fiber length to fiber diameter. For agglomerated fibrous particles like MWCNTs, the aspect ratio using major and minor axes of the enveloping or encompassing ellipse is a measure of elongation of the overall shape of the agglomerate.

Projected area equivalent diameter was defined as the diameter of a sphere with the same project area as the particle of interest. The ImageJ software (ImageJ, U.S. National Institutes of Health, Bethesda, Maryland) was used to perform image analysis to determine project area of the particle. Fig. S1(c) shows the TEM image of the particle processed into a binary image to obtain projected area.

Open area was defined as one minus a ratio of the projected area of the particle to the area of the ellipse which inscribes the particle of interest. This definition is only meaningful for agglomerates. This serves as a measure of porosity or openness of particle structure.

TEM-based projected area-scaling exponent was calculated from TEM images of mobility-classified particles, using the program ImageJ, and the box-counting function. The box-counting method of determining the TEM-based projected area-scaling exponent used a shifting grid algorithm rather than a fixed grid and therefore was more sensitive to the complexity of the surface area (Rasband, 1997–2014). We use a term “projected area-scaling exponent” analogous to 2-D fractal dimension.

3. Experimental methods

3.1. Nanomaterials

Single-walled carbon nanotubes (SWCNTs), multi-walled carbon nanotubes (MWCNTs), functionalized MWCNT, graphene, fullerene, and silver nanorods were studied. Silver nanorods ($L \sim 6.1$ μm, purity 99.9+%; stock : 0475NW2), MWCNT (95+%, OD 10–20 nm, length 10–30 μm; stock : 1205YJ), MWCNT (95+%, OD 60–100 nm, length 5–15 μm; stock : 1234NMG), short MWCNT-OH (95+%, OD 50–80 nm, length 0.5–2.0 μm; stock : 1253YJF) were purchased from Nanostructured & Amorphous Materials, Inc. (Houston, TX), and fullerene (C60, 99.5 wt%) and Graphene nanoplatelets (GNPs, Grade 3) from Cheaptubes Inc. (Brattleboro, VT). The GNP has surface areas 600–750 m^2/g, 4–5 layers, an average thickness of 8 nm, and typical particle diameters of less than 2 μm (Cheaptubes, 2015). SWCNTs were purchased from the Carbon Nanotechnologies, Inc. (CNI, Houston, TX), which were produced by the HiPCO™ technique, employing CO in a continuous-flow gas phase as the carbon feedstock and $Fe(CO)_5$ as the iron containing catalyst precursor. Mitsui MWCNTs was provided from Mitsui & Co. (Ibaraki, Japan). Gold nanorods (OD 25 nm, length 256 nm; part : A12N-25-1400) were purchased from Nanopartz Inc (Loveland, CO). Table 1 summarizes the sources and key properties of nanomaterials used in this study, including the associated abbreviations used in this work to represent them.

3.2. Aerosol generation

Different generation methods were used to aerosolize particles from liquid suspensions and dry powders. The generation methods fall into two categories: dry powder dispersion and liquid-based generation methods. Each nanomaterial was

Table 1
Nanomaterials and aerosolization methods used in this study.

Material	Name	Aerosolization method	Physical size
Single-walled carbon nanotubes (OD 1.4 nm)	SWCNT	Dry dispersion	
Multi-walled carbon nanotubes (OD 10–20 nm)	MWCNT1	Vortex shaking (VS), pneumatic atomization (PA)	Length: 10–30 μm
Multi-walled carbon nanotubes (OD 60–100 nm)	MWCNT2	Vortex shaking	Length: 5–15 μm
Mitsui multi-walled carbon nanotubes (OD 50–60)	MWCNT3	Vortex shaking	Length: 2–3 μm
Functionalized MWCNT (OD 50–80 nm)	MWCNT-OH	Electrospraying (ES)	Length: 0.5–2.0 μm
Silver nanorods	SN	Electrospraying	Length: <6 μm
Fullerene	C60	Electrospraying	
Graphene	Graphene nanoplatelets (GNPs)	Electrospraying	Average thickness: ~8 nm, particle diameter: <2 μm
Gold nanorods (OD 25 nm)	GN	Electrospraying	Length: 256 nm

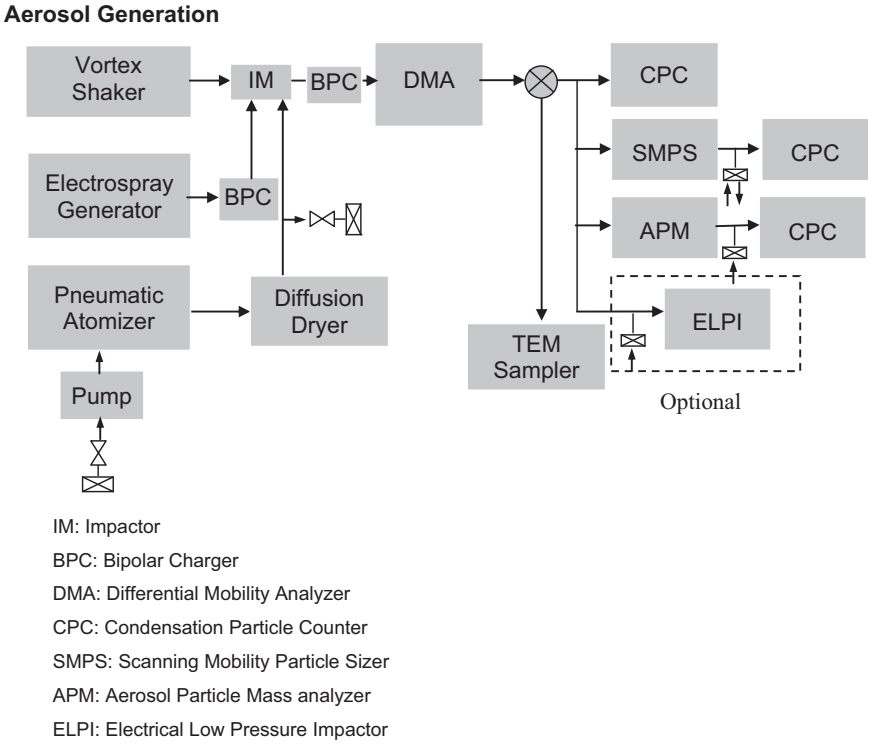

Fig. 1. Experimental setup for particle generation and measurement of particle mobility diameter and mass.

aerosolized using one or all of the following techniques, depending on the amount of material available and the suitability of each technique to generate aerosol with desired characteristics:

1. Vortex shaking (VS)
   Dry dispersion of MWCNTs powders such as MWCNT (OD 10–20 nm), denoted as MWCNT1 in this study, MWCNT (OD 60–100 nm), which is called MWCNT2, and Mitsui MWCNT (OD 50–60 nm), named as MWCNT3, were performed using a vortex shaking method (Ku et al., 2006; Ku, Deye, & Turkevich, 2013). Briefly, a batch of ~0.1 to 1.0 g dry powders were put in a cylindrical glass tube and agitated by a vortex shaker (Vortex Genie 2, Model G560, Scientific Industries Inc., Bohemia, NY, USA). This generation method could produce consistent size distributions with relatively stable number concentrations of airborne MWCNTs for several hours, which was confirmed by measurement of number-size distributions during the entire period of the experiment.

2. Electrospray (ES)
   Suspensions of short MWCNT-OH, graphene, fullerene, and silver nanorods were electrosprayed using an electrospray generator (Ku & Kulkarni, 2009). This technique has the ability to generate monodisperse mobility diameter aerosol particles using small suspension volume, e.g., 1 mL by controlling spraying in a stable cone-jet mode (De la mora & Loscertales, 1994). Each short MWCNT-OH, graphene, fullerene, and silver nanorods were dispersed in ethanol (purity 99.5+, Sigma-Aldrich) and then, sonicated for 5–10 min before use. Suspension concentrations were 25 mg silver nanorods in 1 ml, 0.238 g MWCNT-OH in 20 ml, 0.09 g graphene in 20 ml with trace amount of ammonium acetate, and 0.1 g fullerene (C60) in 20 ml with trace amount of ammonium acetate, respectively.

3. Pneumatic atomization (PA).
   Suspension of the same MWCNT (OD 10–20 nm) used for dry dispersion, i.e., vortex shaking method, was prepared and pneumatically atomized using a constant output atomizer (model 3073, TSI Inc.). These generation techniques together capture a wide range of particle morphology; nebulization resulting in more compact morphologies (due to particle restructuring during droplet evaporation) and the direct dry aerosolization leading to more open structures. The morphology of airborne nanomaterial particles aerosolized during most workplace activities or processes are expected to be somewhere in between the two limits represented by these two techniques (i.e., VS and PA).

3.3. Experimental setup

An experimental approach for determining diffusion and aerodynamic diameter, effective density, and dynamic shape factor of airborne nanomaterial particles is described in this section.

The experimental setup used in this study is shown in Fig. 1. The overall measurement approach involves following steps: (i) generating nanomaterial aerosols, (ii) sending this polydisperse aerosol through a differential mobility analyzer (DMA) to obtain a monodisperse mobility diameter (same as diffusion diameter if particle charge is known) of which is known, (iii) measuring particle mass of DMA-classified aerosol using an aerosol particle mass analyzer (APM), (iv) repeating these measurements for several different mobility diameters in the submicrometer size range, and (v) conducting these measurements for each type of generation technique for the same material or different nanomaterials (i.e. electrospray, pneumatic atomization and dry dispersion) to probe effect of morphology on particle diameters. Experiments were also designed to understand the extent of variability in morphology across nanotube aerosols generated by various techniques such as electrospray, pneumatic atomization, and dry dispersion techniques.

Size distributions of aerosols generated by different methods were measured by a scanning mobility particle sizer (SMPS, Model 3936, TSI Inc., St Paul, MN). Typical aerosol flow rate to the SMPS was 1.0 lpm and sheath flow rates were in the range of 5.0 to 10 lpm depending on desired particle size range and resolution. The DMA-classified aerosol was also collected on a TEM grid using an impactor-based electrostatic precipitator (Ku & Maynard, 2005) for each material to analyze particle morphology and structure. Particle imaging was carried out using a Transmission Electron Microscope. During the TEM analysis, agglomerates were selected and imaged randomly to minimize bias. Magnifications between 60,000× and 100,000× were typically used, giving one to three particles per image. For each sample, five to ten fields of view were used to estimate morphological descriptors for each mobility diameter.

3.4. Particle mass measurement

DMA-classified agglomerates were introduced into an aerosol particle mass analyzer (Ehara, Hagwood, & Coakley, 1996; APM, Model 3600, Kanomax, Inc., Andover, NJ) to obtain an estimate of mean particle mass. The concentration of particles penetrating through the APM is measured as the classifying voltage is changed. Mean mass estimates were obtained (assuming singly charged particles) from using the mass at the peak concentration (Ku et al., 2006; Maynard, Ku, Emery, Stolzenburg, & McMurry, 2007; McMurry et al., 2002). Further details on the APM are described in previous papers (McMurry et al., 2002).

Effective densities, dynamic shape factors, diameter-mass scaling exponents, and aerodynamic diameters of mobility-classified particles were calculated from particle mass and mobility diameter measured using tandem mobility-mass approach, as shown in Eqs. (1) and (4). Direct measurement of the aerodynamic diameters of mobility-classified particles was also made using an electrical low pressure impactor (ELPI) to evaluate the accuracy of the tandem mobility-mass approach for the short MWCNT-OH material (see Fig. S2 in the supplementary information). Aerodynamic diameters of MWCNT-OH from both approaches (APM-based and ELPI) agreed with each other within 22% in the size range tested. Analysis of TEM images was performed to obtain descriptors of morphological characteristics of particles, such as envelop diameter, open area, aspect ratio, and projected area equivalent diameter. The morphological information from the TEM was compared with measured aerodynamic and diffusion diameters of the particles.

4. Results and discussion

4.1. Aerosol generation methods

Typical size distributions of airborne nanomaterials generated by each of three generation methods (VS, PA, and ES) are shown in Fig. S3 of the Supplemental information (SI). Modal diameters for the MWCNT particles (MWCNT1) generated by vortex shaking and liquid atomization are about 100 nm and 60 nm, respectively and it was found that the size distributions and number concentrations are reasonably stable over the test period. Dry dispersion method such as VS produces, in general, well-dispersed aerosol particles from bulk powder, and the degree of agglomeration of generated particles depends on the energy transferred to the bulk powder during mechanical agitation by VS, while the liquid nebulization method generally produces relatively compact aerosol particles (resulting from desolvation of aerosolized droplets), and the agglomeration in gas phase depends on the suspension concentration, droplet size, and droplet evaporation dynamics. It is worth noting that the vortex shaking method produce relatively residue-free size distributions while PA and ES methods generate residue particles (i.e., particles below 30 nm) resulting from soluble species in liquid suspensions. Fig. S3a and b shows that modal diameter of the MWCNT1 particles generated by PA is smaller than that of the same material particles by VS, indicating that the PA-generated particles are more compact due to droplet evaporation dynamics. During the evaporation process, particles inside the droplet restructure or reorganize and shrink as the droplet dries (Ku & Kulkarni, 2009).

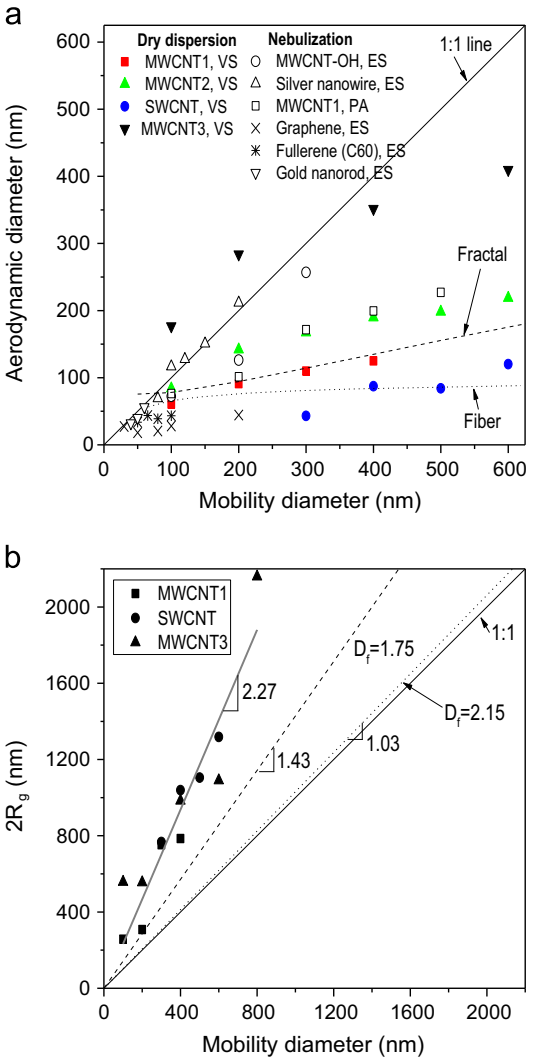

Fig. 2. (a) Aerodynamic diameter vs. mobility diameter for different nanomaterial aerosols (b) Two times radius of gyration vs. mobility diameter. In the legend of the figure (a) VS stands for vortex shaker, ES for electrospray, and PA for pneumatic atomizer. In (a) also shown are curves for idealized fractal and fiber particles. It was assumed that the fractal particles have uniform primary particle size (20 nm) which was the same as the tube diameter of the MWCNT particles. In (b) mass scaling factors for ideal fractal particles (D_f) are included for comparison. The fitting line for measured data was obtained using a model: $y=ax^b$; $a=2.2702\pm1.9028$, $b=1.00519\pm0.1334$, $R^2=0.8604$.

The VS and PA generation methods perhaps can be considered to represent two extremes of morphologies, possibly covering a wide range particle structures of aerosolized nanomaterials produced in various workplace activities.

A vortex shaker (Vortex-Genie 2, Scientific Industries, Inc., Bohemia, NY) was operated at variable speeds of 600–3200 rpm, executing a large ($r=6$ mm) orbit for aggressive vortex shaking. We typically operated the vortex shaker at 70–80% maximum rotation speed. With these operating parameters, the vortex shaking method has provided well-dispersed aerosol particles for different materials, including carbon nanofibers (Ku et al., 2006), MWCNTs (Ku, Deye, Kulkarni, & Baron, 2011), and glass fibers (Ku et al., 2013). Particle size distributions measured during powder bagging operation in a carbon nanofibers (CNF) manufacturing facility have shown agglomerated structures with a dominant modal diameter of 200–250 nm in both mobility and aerodynamic diameters (Evans et al., 2010). The size distributions of the same CNF powder aerosolized by the vortex shaking method in our laboratory showed a similar modal mobility diameter (Ku et al., 2006). An order-of-magnitude analysis indicates that adhesive forces between particles of an agglomerate are about four orders of magnitude higher than the centrifugal force and shear force in a rotating flow, which are separation forces created by vortex shaking that drives particles of the material apart, during vortex agitation, confirming that the VS method used in this study is not capable of breaking apart the agglomerates (see the SI for details). We surmise that the morphology of the particles aerosolized by the VS is perhaps representative of typical workplace activities involving aerosolization via various mechanical agitation methods.

4.2. Measured aerosol properties

Fig. 2a shows aerodynamic diameter as a function of mobility diameter for different nanomaterial aerosols. Only limited number of measurements could be obtained for some particles (e.g. SWCNT, silver nanorods) due to the difficulty in aerosolizing the bulk materials to obtain test aerosol in the desired size and concentration range to allow reliable measurements with acceptable uncertainty.

Curves for idealized fractal and fiber particles are also shown for comparison. Fiber was assumed to be straight and randomly oriented during its transport. Also, it was assumed that the fractal particles have uniform primary particle diameter of 20 nm which was the same as the tube diameter of the MWCNT1 particles studied in this work. The aerodynamic diameter d_{ae} of the fractal particles was calculated from the relationship among d_{ae}, d_{ve} (volume-equivalent diameter), and mobility diameter obtained from the fractal theory where a relation between mobility diameter and number of primary particles is known (Sorensen, 2011; Kulkarni, Baron, Sorensen, & Harper, 2011). d_{ve}, and d_{ae} of the fiber particles were calculated from cylindrical geometry and Cox's theory (Cox, 1970), and mobility diameter was calculated from the

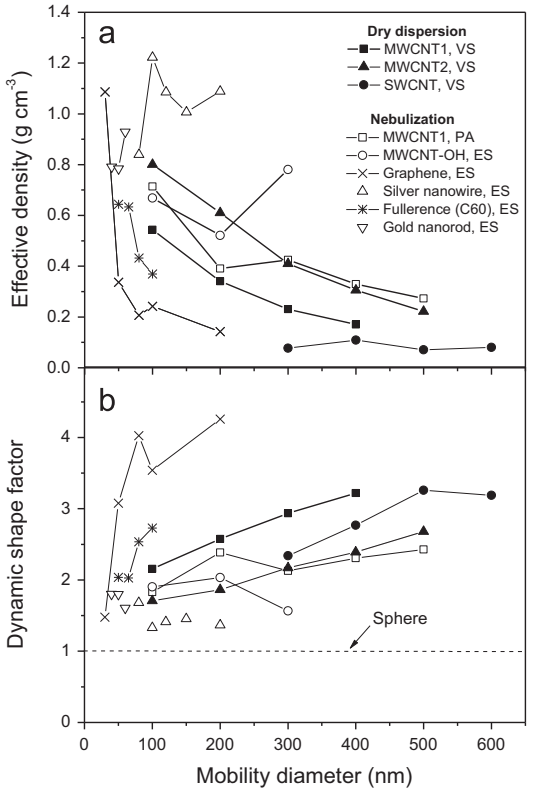

Fig. 3. (a) Effective density as a function of mobility diameter and (b) dynamic shape factor as a function of mobility diameter for different nanomaterial aerosols. In the legend of the figure VS stands for vortex shaker, ES for electrospray, and PA for pneumatic atomizer.

relationship among d_{ae}, d_{ve}, and mobility diameter (Kulkarni et al., 2011). As mobility diameter increases, the aerodynamic diameter also increases. The aerodynamic diameter is smaller than mobility diameter in the size range studied for all nanomaterials except silver and gold nanorods. This is consistent with earlier measurements of other materials (Ku et al., 2006; McMurry et al., 2002; Park et al., 2003). The difference between these two diameters also increases with increasing mobility diameter. For example, the ratio of mobility to aerodynamic diameters of MWCNT1 particles in Fig. 2a generated by vortex shaking is 1.6 at 100 nm and increases to 3.2 at 400 nm. The aerodynamic diameter of silver nanorods and gold nanorods are close to their mobility diameter, perhaps due to their high bulk densities (10.5 g cm^{-3} and 19.3 g cm^{-3} for silver and gold, respectively). Fig. 2b shows radius of gyration calculated from TEM images of three nanomaterials (SWCNT, MWCNT1, Mitsui MWCNT) as a function of mobility diameter. The radius of gyration (R_g) is a measure of distribution of mass around the center of mass within aggregate particle structure. For pure fractals, the radius of gyration, defined as the root mean square radius that quantifies the overall size of the aggregate, is related to mobility diameter and mass scaling factor (Sorensen, 2011). In Fig. 2b the diameter of gyration ($2R_g$) is higher than mobility diameter for all three nanomaterials, which is consistent with similar tendency of large fractal-like agglomerates (Sorensen, 2011). The mass-mobility scaling exponents for diffusion-limited cluster aggregation (DLCA) and reaction-limited cluster aggregation (RLCA) ideal fractal particles (D_f= 1.75 and 2.15, respectively) are also shown in Fig. 2b for comparison. Fig. S4 in the supplementary information (SI) shows particle mass as a function of mobility diameter for the tested materials. The slope of each line in the figure corresponds to mass-diameter scaling exponent (D_f), showing different values compared to fractal dimension of pure, self-

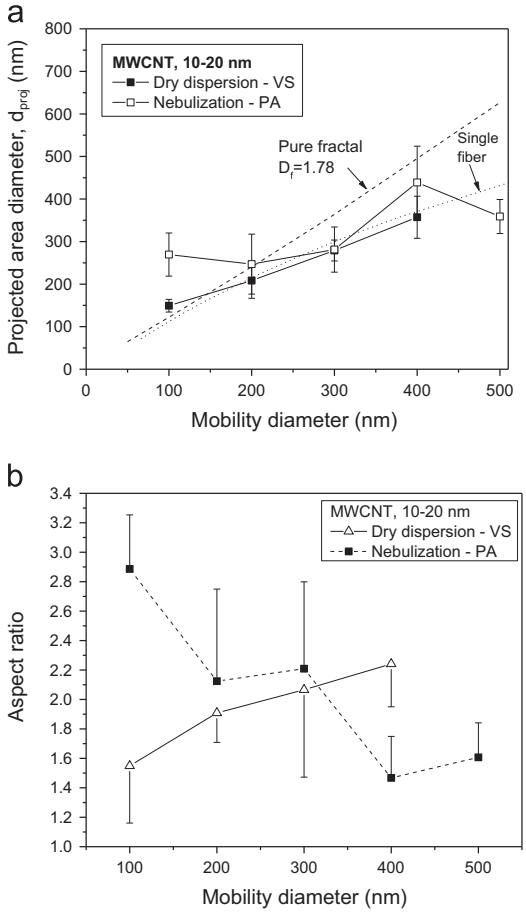

Fig. 4. Characteristic diameter vs. mobility diameter for aerosol particles of the same MWCNT material. (a) Projected area diameter vs mobility diameter for MWCNT-VS and MWCNT-PA and (b) aspect ratios for the aerosols shown in (a). The number in legend box is nominal tube diameter from the manufacturer. Also shown are curves for idealized fractal and fiber particles. Fractal was assumed to be transparent. Fiber was assumed to be straight and randomly oriented. d_{ae} is aerodynamic diameter and d_{proj} is projected area equivalent diameter. It was assumed that the fractal particles have uniform primary particle size (20 nm) which was the same as the tube diameter of the MWCNT particles. Their d_{ve} and d_{proj} was obtained from summation of all primary particle volumes and projected areas of the primary particles, respectively, and d_{ae} was calculated from the relation among d_{ae}, d_{ve}, and mobility diameter obtained from fractal theory where a relation between mobility diameter and number of primary particles is known (Sorensen, 2011; Kulkarni et al., 2011). Also, their d_{ve}, $d_{proj,}$ and d_{ae} of the fiber particles were calculated from cylindrical geometry and Cox's theory (Cox, 1970). The equation for the line for pure fractal in (a) is $d_{proj} = d_{pr}\left[\frac{d_m}{(d_{pr}\cdot(10^{(-2x+0.92)}))}\right]^{1.25}$, where d_{pr} is primary particle diameter, $x = 0.51Kn^{0.043}$, and $Kn = 2\lambda/d_m$ for transition regime (Sorensen, 2011).

similar fractal particles. MWCNT1 generated by vortex shaking has a mass scaling exponent of 2.17 while the same material generated by pneumatic atomization has the exponent of 2.49, indicating that the particles generated by liquid atomization have relatively compact structure. Graphene particles, which have thin planar structure, show the lowest mass scaling exponent of 2.09. Figure S5 in the SI shows TEM images of the tested materials. MWCNT1 aerosol particles generated by vortex shaking show less agglomeration and more open structures as shown in Fig. S5(A). Below 400 nm, as particle size increases, the aspect ratio of the particle increases. On the contrary, the same MWCNT particles generated by pneumatic atomization seem to be highly agglomerated and possess low aspect ratio (Fig. S5(B)). Also, the structure of the particles becomes more compact as particle size increases. Short MWCNT-OH particles seem to be more compact as mobility size increases (Fig. S5(C)). HiPCo process-generated SWCNT particles (Fig. S5(D) in the SI) have a structure with a number of nanoropes and low aspect ratio, while graphene particles show thin planar structures and fullerene (C-60) particles show near-spherical shapes as shown in Fig. S5(E) and (F) in the SI, respectively.

Fig. 3a shows effective densities of the tested materials as a function of mobility diameter. Generally, effective density decreases as mobility diameter increases as expected for most aerosol particles. MWCNT1 (10–20 nm in tube diameter) and MWCNT2 (60–100 nm in tube diameter) particles generated by vortex shaking have effective density decreasing from 0.54 to 0.17 g cm^{-3}, and from 0.80 to 0.19 g cm^{-3}, with increasing diameter from 100 to 500 nm, respectively. The effective density of MWCNT1 particles generated by atomization decreases from 0.71 to 0.27 g cm^{-3} as particle diameter increases from 100 nm to 500 nm, indicating relatively compact structure compared to those generated by vortex shaking. Silver nanorods and gold nanorods have an effective density in the range of 0.84 to 1.22 g cm^{-3} and 0.78 to 0.93 g cm^{-3}, respectively. Considering the bulk material density of silver and gold are 10.5 and 19.2 g cm^{-3} respectively, the effective density of these particles is an order of magnitude smaller than their bulk material densities. Also, short MWCNT-OH particles have higher effective density for larger particles, e.g., 300 nm, unlike other particles, because the particles tend to be highly agglomerated as particle size increases, indicating that those particles are compact and this result is consistent

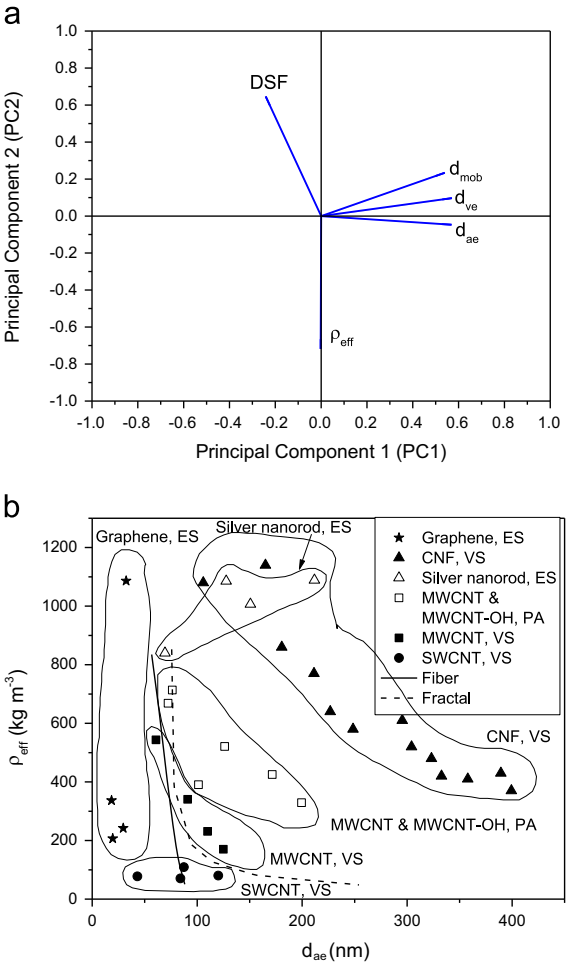

Fig. 5. (a) Loading plot showing relationship between variables in the space of the first two principal components, and (b) effective density (ρ_{eff}) vs. d_{ae}. In plot (a), we clearly see that d_{ae}, d_{ve}, and d_{mob} have heavy loadings for principal component 1, and that ρ_{eff} and DSF have heavy loadings for principal component 2. Plot (b) shows distinct grouping and mapping of data for each material. Data for CNF were obtained from Ku et al. (2006).

Table 2
Mass scaling exponent, dynamic shape factor and open area for nanomaterials tested in this study.

Material	Mass scaling exponent ($D_f^{DMA-APM}$)	Projected area-scaling exponent (D_f^{TEM})	Dynamic shape factor	Open area
SWCNT, VS	2.57		2.34–3.26	–
MWCNT1, VS	2.17	1.43–1.79	2.16–3.22	0.82–0.91
MWCNT1, PA	2.49	1.60–1.91	1.83–2.39	0.68–0.78
MWCNT2, VS	2.46		1.71–2.68	–
MWCNT-OH, ES	3.09	1.64–1.74	1.57–2.03	0.52–0.68
Silver nanorods, ES	2.84		1.33–1.68	–
C60, ES	2.12		2.03–2.73	–
Graphene, ES	2.09	1.86–1.92	1.48–4.02	0.33–0.43
Gold nanorods, ES	2.96		1.60–1.80	–

with TEM image as shown in Fig. S5(C), panel (iii). Furthermore, graphene particles have the lowest effective density among the tested materials, and fullerene (C60) particles having the second-lowest effective density. Effective density of graphene particles at 200 nm was found to be about 0.14 g cm^{-3} and it is smaller than those of MWCNT1 and MWCNT2 at the same size by a factor of 2.4 and 4.3, respectively, due to two-dimensional disk-like structures of graphene particles. Fig. 3b shows dynamic shape factors for various airborne nanomaterial particles. Silver nanorod particles have relatively small dynamic shape factor while MWCNT1 and MWCNT2 particles generated by both vortex shaking and liquid atomization show high dynamic shape factors compared to spheres. Fullerene and graphene particles have much higher dynamic shape factors and particularly, graphene particles show the highest dynamic shape factor. Generally, the dynamic shape factors tend to increase as particle size increases. It is worth noting that in the small size range (below 100 nm), the dynamic shape factor of graphene particles increases rapidly with increasing mobility diameter.

4.3. *Morphological characterization of sampled nanomaterial particles*

Fig. 4a shows projected area equivalent diameter (d_{proj}), as a function of mobility diameter for MWCNT particles of the same material, but generated by different generation methods. The projected area diameter is obtained from TEM image analysis. Curves for idealized fractal and fiber particles are also shown for comparison. Fractal particle was assumed to be transparent (Lall & Friedlander, 2006), which means that nearly entire particle surfaces are exposed to molecular collisions from the surrounding gas. Fiber was assumed to be straight and randomly oriented during its transport. Also, it was assumed that the fractal particles have uniform primary particle diameter of 20 nm which was the same as the tube diameter of the MWCNT1 particles studied in this work. Particle's d_{proj} was obtained from summation of projected areas of all the primary particles, and the number of primary particles was calculated from the fractal theory where a relation between mobility diameter and number of primary particles is known (Kulkarni et al., 2011; Sorensen, 2011). Their d_{ve}, $d_{proj,}$ and d_{ae} of the fiber particles were calculated from cylindrical geometry and Cox's theory (Cox, 1970), and mobility diameter was calculated from the relationship among d_{ae}, d_{ve}, and mobility diameter (Kulkarni et al., 2011). Correlation between d_{proj} and d_{mob} in Fig. 4a for MWCNT-VS is similar to that of single fibers while that for MWCNT-PA is weak. The variability of the projected area for MWCNT-PA is higher than that for MWCNT-VS. It is worth noting that none of these particles exhibit $d_{proj}-d_{mob}$ relationship expected of pure fractal particles. Fig. 4b shows aspect ratios for the aerosols shown in Fig. 4a. The wet (PA) and dry (VS) techniques show opposite trends for aspect ratio as a function of mobility diameter. Aspect ratio of the dry dispersed particles increases with increasing mobility diameter, unlike the particles from PA. The opposite tendency of the aspect ratio for the two particles may be due to particle morphology and structure: the MWCNT-VS particles have longer fibrous structure as mobility size increases (see TEM images in the supplementary material) while the atomized MWCNT particles have short and compact structure. For the MWCNT-PA particles, larger droplets allow more reorganization and restructuring for larger mobility sizes, which reduces the aspect ratio of the particles (see Fig. S6 in the SI for details of characteristic diameter vs. mobility diameter).

Table 2 shows open area of airborne particles for different types of materials. The open area was defined as the ratio of porous area of a smallest ellipse inscribing a particle to projected area of the ellipse. The MWCNT1-VS particles have highest open area and the atomized MWCNTs (MWCNT1-PA) and electrosprayed MWCNTs (MWCNT-OH-ES) are the secondly and thirdly higher in open area among the three different MWCNT materials, respectively. The open area of graphene particles are the lowest among all the materials tested. The open area for each material was found to be 80–90% for the MWCNT1-VS particles, 70–80% for the MWCNT1-PA, 50–70% for the MWCNT-OH-ES, and 35–45% for graphene particles. This suggests that dry dispersion generation method leads to particles with a more open or porous structures compared to liquid-based nebulization. In particular, the MWCNT-OH particles with short length ($\sim$0.5 μm) decrease the open area by making their structure more compact compared to the atomized MWCNT particles with long length ($\sim$10 μm) (see Fig. S6 in the supplementary information for details).

Table 2 also shows comparison of TEM-based projected area-scaling exponent (D_f^{TEM}) with mass-based mass scaling exponent ($D_f^{DMA-APM}$). The TEM-based scaling exponent is derived from two-dimensional (2-D) image, while mass scaling exponent is derived from measured particle mass and therefore is bound by three-dimension (3-D). The 2-D and 3-D D_f (see Fig. S7 in the SI) were obtained for all particle sizes for each material. Three kinds of MWCNT material particles (MWCNT-VS, MWCNT-PA, and MWCNT-OH) show that 2-D projected area-scaling exponent increases with increasing 3-D mass scaling

exponent. The 2-D scaling exponents are 1.59 ± 0.10, 1.78 ± 0.28, and 1.64 ± 0.03, respectively, for MWCNT-VS, MWCNT-PA, and MWCNT-OH. For pure fractals, it has been shown that the projected area fractal dimension is typically 10% less than that determined with the three-dimensional quantities (Kulkarni et al., 2011). However, particles in this study show much higher ratios than those for fractals. Fig. S7 in SI shows comparison of 2-D and 3-D fractal dimensions along with those for pure fractals. The particles tested in this study are not pure fractals; the deviation of the ratio from 1.1 seems to be larger for particles with more compact or dense structure. Unlike the three other materials, the 2-D and 3-D scaling exponents are close to 2, as shown in Fig. S7. This gives a ratio of 3-D to 2-D scaling exponent of 1.11, which agrees well the ratio for pure fractals. A line representing pure fractals with $D_{f,3}/D_{f,2}=1.1$ is shown for comparison. The graphene data fall on this curve.

Estimation of lengths of carbon nanotubes were obtained. Fig. S8 in the supplementary information shows total tube length calculated based on the measured mass (and assumed density) in APM (L_{mass} on y-axis) and on projected area of a particle from TEM images (L_{proj} on x-axis) for different nanomaterials. L_{mass} on y-axis, the total tube length, was obtained with the following equation, $m = A_c L_{mass}\, \rho_p$, where m is particle mass, ρ_p is the particle material density and A_c is the tube cross section area. An average tube diameter (d_t) was used in the calculations based on the actual measurements from several TEM images. L_{proj} on x-axis, the total tube length, was calculated using the relation, $A_{proj} = L_{proj}\, d_t$, where A_{proj} is the particle projected area; the project area was obtained from image processing done by the Image J. The total tube length calculated based on projected area are overestimated for smaller particles while they are underestimated for larger particles compared to those calculated based on measured mass and tube diameter. The underestimation at small mobility diameters in S8 could perhaps be due to multiply charged fraction passing through the DMA that bias the TEM samples, whereas the underestimation at larger particle sizes could be due to significant overlapping of particles in the image. Particles with porous and open structures (mainly those produced from dry dispersion) show better agreement compared to those with compact morphologies (from liquid nebulization). Though SWCNT particles have open and porous structures, they also show significant overlap, leading to underestimation of tube length.

The relevance of morphology of aerosol studied in this work to actual workplace nanomaterial aerosol depends on various factors, including the difference in mechanism of aerosolization (with respect to the energy available for aerosolization and the agglomerate breakup), and alternation of particle morphology post-aerosolization via coagulation with background aerosols (that are not specific to the source of nanomaterials). As noted earlier, the VS method used in this study is likely incapable of breaking the agglomerates apart and perhaps represents most dry dispersion methods involving mechanical agitation. The degree of alteration of particle morphology via coagulation with background aerosol can be significant depending on the particle size distribution of background aerosol. Order-of-magnitude calculations using size distributions of typical ambient/outdoor aerosol size distribution and typical workplace aerosol in nanomaterial manufacturing (available from literature), show that alteration of morphology via coagulation will likely be insignificant in many cases (see for example the SI for order-of-magnitude analysis). For most workplaces, where airborne nanomaterial is the dominant source of aerosol, the range of morphologies studied in this work are likely to be relevant.

It is expected that high aspect-ratio particle orientation in electric field plays an important role in determining the mobility diameter. To investigate the particle orientation effect, we compared measured mobility diameter and aspect ratio with theoretically calculated values based on Li et al. (2013) and Lall and Friedlander (2006) works, respectively. Some of the results are as shown in Fig. S9 of the supplemental information: the results (Fig. S9(a)) show that mobility diameters predicted by theory for MWCNT1 (VS) agree reasonably with measured diameters at smaller mobility diameter (i.e. less than 200 nm) for randomly oriented MWCNT particles in the free molecular regime. But, the predicted values overestimate the measured ones at mobility diameter larger than 200 nm, at which aligned MWCNT particles better predicts than randomly oriented particles.

Fig. S9(b) shows the relationship between aspect ratio and mobility diameter calculated based on the friction coefficient equation, compared to experimental results. Aspect ratios (these are equal to number of primary particles for chain-like agglomerates) agree well with the experimental values up to 200 nm in mobility diameter and deviate somewhat for MWCNT1 (VS), and deviate significantly for MWCNT1 (PA). This may be due to heavy agglomeration of MWCNT1 (PA) particles.

4.4. Principal components analysis (PCA)

We performed PCA on the measured properties to identify minimum set of orthogonal particle properties that could be used to clarify or distinguish different nanomaterials. We applied PCA to the entire data set that included the following measured or deduced particles properties: mobility diameter, aerodynamic diameter, volume equivalent diameter, mass, effective density, dynamic shape factor, and friction coefficient.

Fig. 5(a) shows a loading plot for the first two principal components based on principal component analysis (PCA). The variance accounted for by each of the components is its associated eigenvalue. The eigenvectors with large eigenvalues contain most of the information. Most of the variance in our data could be accounted for by the first two components (the first principal component (PC1) about 60.2%; the second component (PC2) about 37.5%). Fig. 5(a) shows relationship between five different variables (i.e., d_{ae}, d_{ve}, d_{mob}, ρ_{eff}, and DSF) in the eigenvector space of PC1 and PC2; d_{ae}, d_{ve}, and d_{mob} have heavy loadings along PC1. On the other hand, ρ_{eff} and DSF have heavy loadings along PC2 and capture information largely independent of d_{ae}, d_{ve}, d_{mob}. We used aerodynamic diameter (d_{ae}) and effective density (based on d_{mob}; ρ_{eff}) as surrogates for PC1 and PC2 and plotted the data of ρ_{eff} as a function of d_{ae} as shown in Fig. 5(b). Table 3 summarizes results of curve fitting for effective density vs. aerodynamic diameter shown in Fig. 5(b). Model equation for the fitting was $\rho_{eff} = a * d_{ae}^{b}$. Each material tested, falls into one of three distinct groups or clusters that define the relationship between the

Table 3
Fitting curves for effective density vs. aerodynamic diameter for different nanomaterials.

Model equation	$\rho_{eff} = a * d_{ae}^{b}$				
Nanomaterial	Parameter, a	Parameter, b	R^2	Observations	p-Value
MWCNT1, VS	246176.7	−1.48802	0.99274	4	0.004
MWCNT1 and MWCNT-OH, PA	10537.1	−0.6452	0.69701	6	0.048
CNF, VS	47468.4	−0.78436	0.82248	13	3.01E−06
SWCNT, VS	58.7	0.08343	0.03284	4	0.867
Silver nanorods, ES	326.9	0.2298	0.7786	4	0.190
Graphene, ES	2.6754	1.5444	0.3449	4	0.162

two PCs: (1) exponent b is negative, e.g., in the range between −1.49 and −0.65, for MWCNT1-VS, CNF-VS, and MWCNT1 and MWCNT-OH, (2) the exponent is positive, e.g. for graphene, and (3) the exponent is close to zero, e.g., for SWCNT and silver nanorods. The particles in the first group (with negative exponent) have highly non-spherical fibrous structure with relative high aspect ratios. The friction drag on these particles increases with increasing aspect ratio, giving rise to negative exponent. The second group of particles (b is positive) correspond to thin planar structures like graphenes. For these particles, overall mass of the agglomerate significantly increases with increasing mobility size, compared to the increase in the drag. For further confirmation of the relationship $\rho_{eff} = a * d_{ae}^{b}$, we combined Eqs. (1) and (2) to obtain the functional relation of effective density with aerodynamic diameter. The comparison of exponent b from this and exponent in Table 3 is summarized in the supplemental information (Table S1) for these nanomaterials. Both parameters b (exponent) show qualitatively similar trends except SWCNT. The large difference for SWCNT may be due to the very disparate mobility and aerodynamic diameters.

The particles belonging to the third group of particles (b is close to zero) have low aspect ratio structure. These particles are characterized by low inertia and their effective density does not substantially change with increasing agglomerate size. An alternative representation using DSF and particle mass as orthogonal components shows similar grouping of nanomaterials (see Fig. S10 in the SI for the plot of DSF vs. mass) and can be used as an alternate set of eigenvectors.

The complete dataset for particle properties measured in this study is included in the supplemental information (Table S2).

5. Conclusions

Airborne engineered nanomaterials such as single-walled carbon nanotubes (SWCNTs), multi-walled carbon nanotubes (MWCNTs), functionalized MWCNT, graphene, fullerene, silver and gold nanorods were characterized using a tandem system of a differential mobility analyzer and an aerosol particle mass analyzer to obtain their airborne transport properties and compare those to morphological descriptors based on transmission electron microscopy (TEM) images. From the measurement of mobility diameter, particle mass, and TEM analysis, equivalent diameters such as aerodynamic diameter, envelope diameter and projected-area diameter, effective density, dynamic shape factor, mass scaling exponent and open area of the particles were obtained in the submicrometer size range. In addition, principal component analysis was used to show that aerodynamic diameter and effective density (based on mobility diameter) can be used as two orthogonal particle properties that capture key transport properties of interest for most particle deposition systems. The exponent b, which defines the correlation between ρ_{eff} and d_{ae} ($\rho_{eff} \sim d_{ae}^{b}$) could be used to classify materials in three distinct groups with different characters. Aerodynamic diameter was found to be smaller by a factor of 2–4 than mobility diameter for all nanomaterials studied in this work except silver and gold nanorods below 500 nm, emphasizing the need to use mechanism-specific equivalent diameters when modeling particle deposition in respiratory system or in other engineering systems such as particulate filters. Comparison with fractal theory showed that the particles agglomerates of aerosolized nanomaterials are not pure fractals.

Disclaimer

The mention of any company or product does not constitute an endorsement by the Centers for Disease Control and Prevention. The findings and conclusions in this paper are those of the authors and do not necessarily represent the views of the National Institute for Occupational Safety and Health.

Acknowledgments

The authors would like to thank Mr. Greg Deye and Dr. Chen Wang at NIOSH for helpful discussions on this work, and Joe Fernback for TEM images. This work was funded by the National Institute for Occupational Safety and Health through the Nanotechnology Research Center (NTRC) program (Project CAN 927ZJLS).

Appendix A. Supplementary information

Supplementary data associated with this article can be found in the online version at doi:10.1016/j.jaerosci.2015.09.001.

References

Anjilvel, S., & Asgharian, B. (1995). A multiple-path model of particle deposition in the rat lung. *Fundamental and Applied Toxicology*, *28*, 41–50.

Baron, P. A., Deye, G. J., Chen, B. T., Schwegler-Berry, D. E., Shvedova, A. A., & Castranova, V. (2008). Aerosolization of single-walled carbon nanotubes for an inhalation study. *Inhalation Toxicology*, *20*, 751–760.

Baughman, R. H., Zakhidov, A. A., & de Heer, W. A. (2002). Carbon nanotubes—The route toward applications. *Science*, *297*, 787–792.

Birch, M. E., Ku, B. K., Evans, D. E., & Ruda-Eberenz, T. A. (2011). Exposure and emissions monitoring during carbon nanofiber production—Part I: Elemental carbon and iron-soot aerosols. *Annals of Occupational Hygiene*, *55*, 1016–1036.

Cheaptubes, Inc. (2015). ⟨http://www.cheaptubesinc.com/graphene-nanoplatelets.htm⟩.

Cox, R. G. (1970). The motion of long slender bodies in a viscous fluid I: General theory. *Journal of Fluid Mechanics*, *44*, 791.

De la mora, J. F., & Loscertales, I. G. (1994). The current emitted by highly conducting Taylor cones. *Journal of Fluid Mechanics*, *260*, 155–184.

Ehara, K., Hagwood, C., & Coakley, K. J. (1996). Novel method to classify aerosol particles according to their mass-to-charge ratio—Aerosol particle mass analyzer. *Journal of Aerosol Science*, *27*, 217–234.

Evans, D. E., Ku, B. K., Birch, M. E., & Dunn, K. H. (2010). Aerosol monitoring during carbon nanofiber production: Mobile direct-reading sampling. *Annals of Occupational Hygiene*, *52*, 9–21.

Hajipour, M. J., Fromm, K. M., Ashkarran, A. A., de Aberasturi, D. J., de Larramendi, I. R., et al. (2012). Antibacterial properties of nanoparticles. *Trends in Biotechnology*, *30*(10), 499–511.

Hinds, W. C. (1999). *Aerosol technology: Properties, behavior, and measurement of airborne particles*. New York, USA: John Wiley & Sons.

ICRP (International Commission on Radiological Protection). (1994). *Human respiratory tract model for radiological protection*. Oxford: Pergamon Press, Elsevier Science Ltd. [ICRP Publication 66]

Kasper, G. (1982). Dynamics and measurement of smokes.1. Size characterization of non-spherical particles. *Aerosol Science and Technology*, *1*, 187–199.

Kisin, E. R., Murray, A. R., Sargent, L., Lowry, D., Chirila, M., Siegrist, K. J., … Shvedova, A. A. (2011). Genotoxicity of carbon nanofibers: Are they potentially more or less dangerous than carbon nanotubes or asbestos?. *Toxicology and Applied Pharmacology*, *252*, 1–10.

Ku, B. K., & Kulkarni, P. (2009). Morphology of single-wall carbon nanotube aggregates generated by electrospray of aqueous suspensions. *Journal of Nanoparticle Research*, *11*, 1393–1403.

Ku, B. K., & Maynard, A. D. (2005). Comparing aerosol surface-area measurements of monodisperse ultrafine silver agglomerates by mobility analysis, transmission electron microscopy and diffusion charging. *Journal of Aerosol Science*, *36*, 1108–1124.

Ku, B. K., Emery, M. S., Maynard, A. D., Stolzenburg, M. R., & McMurry, P. H. (2006). In situ structure characterization of airborne carbon nanofibres by a tandem mobility-mass analysis. *Nanotechnology*, *17*, 3613–3621.

Ku, B. K., Deye, G., & Turkevich, L. A. (2013). Characterization of a vortex shaking method for aerosolizing fibers. *Aerosol Science and Technology*, *47*(12), 1293–1301, http://dx.doi.org/10.1080/02786826.2013.836588.

Ku, B. K., Deye, G. J., Kulkarni, P., & Baron, P. A. (2011). Bipolar diffusion charging of high-aspect ratio aerosols. *Journal of Electrostatics*, *69*(6), 641–647.

Kulkarni, P., Baron, P. A., Sorensen, C., & Harper, M (2011). Nonspherical particle measurement: shape factor, fractals, and fibers. In: P. Kulkarni, P. A. Baron, K. Willeke (Eds.) *Aerosol measurement: principles, techniques, and applications*, 3 ed.

Lall, A. A., & Friedlander, S. K. (2006). On-line measurement of ultrafine aggregate surface area and volume distributions by electrical mobility analysis: I. Theoretical analysis. *Journal of Aerosol Science*, *37*(3), 260–271.

Li, M., You, R., Mulholland, G. W., & Zachariah, M. R. (2013). Evaluating the Mobility of Nanorods in Electric Fields. *Aerosol Science and Technology*, *Aerosol Science and Technology*(10), 1101–1107.

Maynard, A. D., Baron, P. A., Foley, M., Shvedova, A. A., Kisin, E. R., & Castranova, V. (2004). Exposure to carbon nanotube material: Aerosol release during the handling of unrefined single-walled carbon nanotube material. *Journal of Toxicology and Environmental Health—Part A*, *67*, 87–107.

Maynard, A. D., Ku, B. K., Emery, M., Stolzenburg, M., & McMurry, P. H. (2007). Measuring particle size-dependent physicochemical structure in airborne single walled carbon nanotube agglomerates. *Journal of Nanoparticle Research*, *9*, 85–92.

McMurry, P. H., Wang, X., Park, K., & Ehara, K. (2002). The relationship between mass and mobility for atmospheric particles: A new technique for measuring particle density. *Aerosol Science and Technology*, *36*, 227–238.

Mercer, R. R., Scabilloni, J. F., Hubbs, A. F., Battelli, L. A., McKinney, W., Friend, S., … Porter, D. W. (2013). Distribution and fibrotic response following inhalation exposure to multi-walled carbon nanotubes. *Particle and Fibre Toxicology*, *10*, 33.

Nanoamor, Inc. (2015). *NanoAmor carbon nanotubes and nanofibers, graphene*. Retrieved from: ⟨http://www.nanoamor.com/carbon_nanotubes___nanofibers__graphene⟩.

NIOSH. (2009). *Approaches to safe nanotechnology: managing the health and safety concerns associated with engineered nanomaterials*. [DHHS (NIOSH) Publication No. 2009–2125]⟨http://www.cdc.gov/niosh/docs/2009-125/pdfs/2009-125.pdf⟩.

NIOSH. (2013). *Occupational exposure to carbon nanotubes and nanofibers: Current intelligence bulletin 65*. [DHHS (NIOSH) Publication No. 2013–2145].

Novoselov, K. S., Fal'ko, V. I., Colombo, L., Gellert, P. R., Schwab, M. G., & Kim, K. (2012). A roadmap for graphene. *Nature*, *490*, 192–200.

Park, K., Cao, F., Kittelson, D. B., & McMurry, P. H. (2003). Relationship between particle mass and mobility for diesel exhaust particles. *Environmental Science and Technology*, *37*, 577–583.

Rasband, W.S. (1997–2014). *ImageJ*. U.S. National Institutes of Health, Bethesda, Maryland, USA. ⟨http://imagej.nih.gov/ij/⟩.

Sargent, L. M., Porter, D. W., Staska, L. M., Hubbs, A. F., Lowry, D. T., Battelli, L., … Reynolds, S. H. (2014). Promotion of lung adenocarcinoma following inhalation exposure to multi-walled carbon nanotubes. *Particle and Fibre Toxicology*, *11*, 3.

Schmidt-ott, A., Baltensperger, U., Gaggeler, H. W., & Jost, D. T. (1990). Scaling behavior of physical parameters describing agglomerates. *Journal of Aerosol Science*, *21*, 711–717.

Shvedova, A. A., Kisin, E. R., Mercer, R., Murray, A. R., Johnson, V. J., Potapovich, A. I., … Baron, P. (2005). Unusual inflammatory and fibrogenic pulmonary responses to single-walled carbon nanotubes in mice. *American Journal of Physiology—Lung Cellular and Molecular Physiology*, *289*, L698–L708.

Sorensen, C. M. (2011). The mobility of fractal aggregates: A review. *Aerosol Science and Technology*, *45*, 765–779.